NJC
New Journal of Chemistry
A journal for new directions in chemistry

Accepted Manuscript

This article can be cited before page numbers have been issued, to do this please use: L. Ruiyi, M. Li and Z. Li, *New J. Chem.*, 2025, DOI: 10.1039/D5NJ02639C.

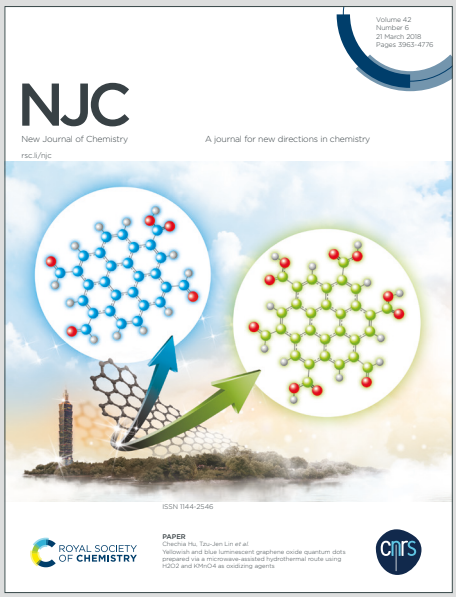

This is an Accepted Manuscript, which has been through the Royal Society of Chemistry peer review process and has been accepted for publication.

Accepted Manuscripts are published online shortly after acceptance, before technical editing, formatting and proof reading. Using this free service, authors can make their results available to the community, in citable form, before we publish the edited article. We will replace this Accepted Manuscript with the edited and formatted Advance Article as soon as it is available.

You can find more information about Accepted Manuscripts in the Information for Authors.

Please note that technical editing may introduce minor changes to the text and/or graphics, which may alter content. The journal's standard Terms & Conditions and the Ethical guidelines still apply. In no event shall the Royal Society of Chemistry be held responsible for any errors or omissions in this Accepted Manuscript or any consequences arising from the use of any information it contains.

View Article Online
DOI: 10.1039/D5NJ02639C

ARTICLE

Gln-GQD-Enabled FeCoNiCuAu$_{0.5}$-High Entropy Alloy Nanoparticles for Ultrasensitive and Non-Invasive Electrochemical Uric Acid Detection

Received 00th January 20xx,
Accepted 00th January 20xx

DOI: 10.1039/x0xx00000x

Li Ruiyi, Li Mingyao and Li Zaijun*

The limited sensitivity restricts the practical application of present electrochemical sensors for detection of uric acid in human sweat. The paper reported one approach for construction of FeCoNiCuAu$_{0.5}$ high-entropy alloy nanoparticles (FeCoNiCuAu$_{0.5}$-HEA) by introducing glutamine-functionalized graphene quantum dot (Gln-GQD). Fe^{3+}, Co^{2+}, Ni^{2+} and Cu^{2+} are combined with Gln-GQD to form stable complex, which sebsequently coordinated with Au^{3+}. Followed by two-stage thermal annealing in N_2 atmosphere. The resulting FeCoNiCuAu$_{0.5}$-HEA shows one spherical nanostructure with small particle size of 47.5±0.63 nm, FCC and BCC phase, and uniform distribution of all metal elements. The HEA nanoparticles are well dispered on the three-dimensional graphene framework formed by graphene sheets intertwining each other. The integration of five metal element mixture and Gln-GQD introduction achieves to excellent electron/ion conductivity, good affinity with ploar electrolyte, and significantly enhanced catalytic activity. The catalytic activity is more than 2.7 times of gold nanoparticles. The FeCoNiCuAu$_{0.5}$-HEA-based sensor offers an ultrasensitive electrochemical response towards uric acid. The differential pulse voltammetric peak current will linearly increase with the increase of uric acid concentration in the range of 0.01-1 μM uric acid with a detection limit of 4.3×10^{-9} M (S/N=3). The as-proposed analytical method provides the advantage of high sensitivity, selectivity and repeatability for detection of uric acid in human sweat.

1 Introduction

Uric acid, the terminal catabolite of human purine metabolism derived from both endogenous cellular turnover and exogenous dietary sources, serves as a pivotal biomarker with significant physiological and pathological implications.[1] Its concentration exhibits substantial heterogeneity across biological matrices. However, elevated serum uric acid levels (hyperuricemia) pose serious health risks, being strongly linked to multisystem morbidity including chronic kidney disease, type II diabetes mellitus, cardiovascular pathologies, and gout.[2] The alarming global escalation of hyperuricemia over the past decade, driven by dietary shifts and lifestyle changes, underscores the critical need for effective monitoring. Conventional detection methods, while clinically used, often lack sufficient sensitivity and specificity, particularly in complex biological samples or patients with renal impairment.[3] This highlights the urgent necessity for innovative biosensing platforms. Analyzing uric acid in sweat emerges as a particularly promising approach due to its potential for non-invasive, rapid, and frequent monitoring. Reliable sweat-based quantification, enabled by advancements in electrochemical or nano-engineered assays, could bridge the current translational gap. It offers a pathway for point-of-care testing, early detection of rising levels, and personalized management of hyperuricemia and its associated comorbidities, ultimately improving patient outcomes.[4]

Several methodologies are currently employed for uric acid detection, each presenting distinct advantages and limitations. Colorimetric assays offer simplicity and rapidity but are hampered by low sensitivity, rendering them unsuitable for trace-level analysis in biological fluids. Liquid chromatography-mass spectrometry (LC-MS),[5] while the laboratory gold standard for quantification, is impractical for point-of-care applications due to its bulky instrumentation and requirement for operator expertise. Surface-enhanced Raman scattering (SERS)[6] and fluorescence-based methods[7] provide high sensitivity and selectivity but remain vulnerable to environmental interference, potentially compromising reliability. In contrast, electrochemical sensors emerge as the most promising approach due to their rapid response, high sensitivity, inherent miniaturization potential, and suitability for portable devices.[8] These sensors often utilize the enzyme uricase for specificity, yet face significant challenges including intricate enzyme immobilization protocols and strict operational constraints, which impact stability and reproducibility.[9] Consequently, while electrochemical sensors represent the ideal platform for uric acid sensing, particularly for decentralized testing, their current sensitivity is insufficient for reliably quantifying uric acid in sweat. Sweat contains uric acid at significantly lower concentrations (typically micromolar range) compared to serum or urine, demanding ultra-high sensitivity.[10] The limitations of enzyme-based systems directly hinder achieving the necessary performance in this

*Key Laboratory of Synthetic and Biological Colloids, Ministry of Education, School of Chemical and Material Engineering, School of Life Science and Health Engineering, Jiangnan University, Wuxi 214122, China
†Footnotes relating to the title and/or authors should appear here.
Supplementary Information available: [details of any supplementary information available should be included here]. See DOI: 10.1039/x0xx00000x

View Article Online
DOI: 10.1039/D5NJ02636G

complex, dilute matrix. Therefore, as highlighted in the text, developing non-enzymatic, enzyme-mimetic nanomaterials has become a pivotal strategy to overcome these sensitivity barriers and enable robust electrochemical detection of uric acid in sweat for practical applications.

Development of effective sensing materials for electrochemical uric acid detection, particularly in complex matrices like human sweat, faces significant challenges despite advances in several material classes. Carbon-based nanomaterials such as carbon nanotubes,[11] graphene[12] and MXene[13] offer superior electrical conductivity and mechanical stability but lack intrinsic catalytic selectivity for uric acid oxidation. Metal oxides such as ZnO,[14] Co_3O_4[15] and CuO[16] provide targeted catalytic activity but suffer from inherently poor electrical conductivity, limiting electrochemical signal amplification. Noble metal nanoparticles such as Au,[17] Pt[18] and Pd[19] combine high conductivity with catalytic efficiency; however, their practical scalability and widespread application are severely hindered by resource scarcity and prohibitive costs. Consequently, designing cost-effective, robust, and selective sensing materials remains a major hurdle. High-Entropy Alloy (HEA) nanoparticles, composed of five or more metallic elements forming single-phase solid solutions, have emerged as promising candidates due to their multifunctionality, excellent catalytic activity, and tunable selectivity via elemental configuration.[20] However, three critical limitations currently impede their practical application for sweat-based uric acid sensing: (1) Existing synthesis methods are unsuitable for large-scale production, requiring specialized equipment and harsh conditions; (2) The catalytic activity of current HEA nanoparticles remains inferior to benchmark noble metals; and (3) Their inherent hydrophobicity results in poor affinity for polar analytes and redox probes in aqueous biological environments like sweat. These substantial barriers underscore the urgent need to develop novel HEA-based sensing materials capable of overcoming these specific limitations. Addressing these challenges—achieving scalable synthesis, enhancing catalytic performance to rival noble metals, and improving hydrophilicity—is essential to fully exploit HEA's potential for enabling sensitive, selective, and practical electrochemical uric acid detection in human sweat.

This study reports the synthesis of $FeCoNiCuAu_{0.5}$ high-entropy alloy nanoparticles ($FeCoNiCuAu_{0.5}$-HEA) facilitated by glutamine-functionalized graphene quantum dot (Gln-GQD). The integration of the five-component metal system with Gln-GQDs yields ultrahigh catalytic activity, exceeding that of Au nanoparticles by more than 2.7-fold. Furthermore, the $FeCoNiCuAu_{0.5}$-HEA-based sensor demonstrates high sensitivity, selectivity, and repeatability for uric acid detection in human sweat.

2 Experimental

2.1 Synthesis of Gln-GQD

Gln-GQD was synthesized following a previously established protocol.[21] Briefly, citric acid (25 g) and L-glutamine (Gln, 19.02 g) were thoroughly mixed and reacted at 160 °C for 4 hours under vigorous stirring. Subsequently, the resulting mixture was centrifuged at 8000 rpm for 10 minutes to remove insoluble aggregates and large carbonaceous sheets. The supernatant was then dialyzed against deionized water using a membrane with a molecular weight cut-off (MWCO) of 1000 Da for 12 hours to eliminate residual unreacted precursors and low-molecular-weight impurities. Finally, the purified solution was lyophilized to obtain the Gln-GQD product.

2.2 Synthesis of $FeCoNiCuAu_{0.5}$-HEA

$FeCoNiCuAu_{0.5}$-HEA was synthesized via two-stage coordination followed by two-stage thermal annealing. In a typical procedure, $Fe(NO_3)_3{\cdot}9H_2O$ (0.02 mol), $Co(NO_3)_2{\cdot}6H_2O$ (0.02 mol), $Ni(NO_3)_2{\cdot}6H_2O$ (0.02 mol), and $Cu(NO_3)_2 \cdot 3\,H_2O$ (0.02 mol) were mixed. The mixed solution was dropped into 50 mL of 100 mg mL^{-1} Gln-GQD aqueous solution under vigorous stirring. After 2 h of stirring, added $HAuCl_4{\cdot}xH_2O$ (0.01 mol) into the above solution. Followed by stirring for 2 h and vacuum spray drying. To obtain $FeCoNiCuAu_{0.5}$-HEA, the collected Me-Gln-GQD complex was thermally annealed under N_2 flow. This annealing includes a low-temperature stage (400°C for 2 h with heating rate of 1 °C min^{-1}) followed by a high-temperature stage (800 °C for 2 h with heating rate of 5 °C min^{-1}). In addition, one control sample—Au NP was synthesized by omitting $Fe(NO_3)_3{\cdot}9H_2O$, $Co(NO_3)_2{\cdot}6H_2O$, $Ni(NO_3)_2{\cdot}6H_2O$ and $Cu(NO_3)_2 \cdot 3\,H_2O$.

2.3 Sensor Construction

A homogeneous dispersion of $FeCoNiCuAu_{0.5}$-HEA (1 mg mL^{-1}) was uniformly blended with an equal volume of chitosan solution (5 wt.%) under magnetic stirring (500 rpm) to synthesize $FeCoNiCuAu_{0.5}$-HEA/chitosan composite dispersion. For electrode modification, a precisely measured 5 μL aliquot of this dispersion was drop-cast onto a polished glassy carbon electrode (GCE, 2-mm diameter) and air-dried at controlled ambient conditions (25 ± 1°C, RH < 30%). Subsequently, 5 μL of 1 mM mercaptohexanol (MCH) solution was uniformly applied to the modified surface and incubated for 2 hours (>80% RH) to facilitate thiol-mediated self-assembly formation, thereby establishing a dense monolayer that blocks non-specific binding sites and optimizes electrode/electrolyte interface characteristics. Following this modification, the electrode underwent rigorous rinsing with ≥18.2 MΩ cm^{-1} ultrapure water (3 cycles) to remove unbound molecules, gentle drying under high-purity nitrogen (99.999%), and final storage at 4°C in a sealed light-proof container to ensure interfacial stability prior to electrochemical testing.

2.4 Electrochemical Detection of Uric Acid

Standard uric acid solutions or test samples (1.0 mL) were precisely mixed with 5.0 mL of phosphate-buffered saline (PBS, 0.1 M, pH 7.4) through vortex agitation (2,500 rpm, 30 s) to ensure homogeneity. The resultant mixture was subjected to rigorous degassing via argon bubbling (99.999% purity, 20 min) followed by 5 min of static equilibrium to establish an oxygen-depleted electrochemical environment. Cyclic voltammetry (CV) and differential pulse voltammetry (DPV) measurements were subsequently performed in an air-tight three-electrode cell maintained under continuous argon blanket. Scan parameters were optimized as follows: CV at 50 mV s^{-1} scan rate (potential

View Article Online
DOI: 10.1039/D5NJ02639G

window: -0.2 to +0.6 V vs. Ag/AgCl), DPV with 10 mV step potential, 50 ms pulse width, and 0.2 s pulse period. All experiments were conducted at 25.0 ± 0.5°C using an electrochemical workstation with Faraday cage isolation to minimize external interference and electrode history effects.

3 Results and Discussions

3.1 Material Design Rationale and Synthesis Mechanism

Design and synthesis strategy of Gln-GQD and $FeCoNiCuAu_{0.5}$-HEA were presented at **Fig. 1**. Firstly, Gln-GQD was made via single-step pyrolysis of citric acid and glutamine (Gln). The Gln incorporation as a co-precursor during citric acid carbonization critically modifies the physicochemical and biological properties of Gln-GQD. Mechanistically, Gln introduces nitrogen heteroatoms and multifunctional coordination sites (-COOH, -OH, $-NH_2$) into the carbon lattice of graphene sheets during the pyrolysis, which fundamentally alters the reaction pathway compared to citric acid-derived GQDs. This co-carbonization process generates a heterogeneous mixture, necessitating centrifugal separation (8,000 rpm, 10 min) to isolate quantum-confined fraction by removing insoluble aggregates and large carbon sheets, thereby refining the size distribution. Subsequent dialysis (1,000 Da MWCO) further purifies nano-scale particles while retaining Gln-derived surface functionalities. These nitrogen-enriched groups (amides) synergize with oxygen moieties to create a highly functionalized surface, substantially enhancing multicoordination capability for metal ions and electron transfer efficiency—properties essential for the subsequent formation of $FeCoNiCuAu_{0.5}$-HEA. Furthermore, Gln's biological origin as a native amino acid, coupled with the hydrophilic surface termination (-COOH, -OH, $-NH_2$) and rigorous removal of low-MW impurities via dialysis, confers inherent biocompatibility potential by promoting aqueous dispersibility and reducing cytotoxic risks in biological environments. Thus, the Gln incorporation transcends mere doping; it enables a tailored interface design that concurrently optimizes nanoscale dimensions, surface reactivity, and biological integration.

The formed Gln-GQD was used for synthesis of $FeCoNiCuAu_{0.5}$-HEA. The HEA integrates Au (primary catalytic center) with four consecutive 4th-period transition metals (Fe, Co, Ni, Cu; Z=23-26), employing a 50% atomic proportion of Au relative to other constituents for cost optimization. The electronic configuration continuity across Fe-Co-Ni-Cu enables low-energy-barrier d-orbital hybridization, inducing electron density delocalization and active-site optimization. This synergistic configuration overcomes activity-selectivity limitations inherent to monometallic Au catalysts.[22]

One sequential coordination-thermal protocol was implemented for the combination of Gln-GQD with metal ions. First, transition metal ions (Fe^{3+}, Co^{2+}, Ni^{2+}, Cu^{2+}) were complexed with Gln-GQD prior to controlled Au^{3+} introduction, achieving kinetic suppression of premature Au^0 nucleation. The sequential coordination strategy fundamentally redefines atomic-level mixing by exploiting multifunctional scaffold of Gln-GQD to enforce pre-alloying spatial order. Unlike conventional co-reduction where simultaneous metal reduction induces kinetic segregation (especially between Au^{3+} and base metals), this protocol first anchors $Fe^{3+}/Co^{2+}/Ni^{2+}/Cu^{2+}$ ions to Gln-GQD's coordination sites (-COOH, $-NH_2$), creating a uniformly dispersed "molecular blueprint". Controlled introduction of Au^{3+} thereafter capitalizes on the suppressed reduction kinetics within this pre-organized matrix, preventing preferential Au^0 nucleation. This stepwise confinement ensures all five metals achieve atomic dispersion prior to reduction—a critical innovation that eliminates nucleation disparities and precludes phase-separated intermediates inherent to single-pot syntheses.

Subsequent two-stage annealing comprised: (i) Precursor formation at 400 °C (1 °C min^{-1}) enabling kinetically-controlled reduction without elemental segregation; (ii) Rapid heating to 800 °C (5 °C min^{-1}) triggering explosive Gln-GQD decomposition where evolved gases drove confined-space atomic effusion and high-entropy-stabilized alloying. The two-stage annealing transforms thermodynamic limitations into stabilization opportunities through a gas-dynamically mediated entropy surge. During the 400°C pre-annealing, Gln-GQD's carbon framework maintains atomic proximity during kinetically controlled reduction, generating a metastable precursor alloy without elemental de-mixing. The subsequent rapid ramp to 800°C triggers explosive decomposition of the Gln-GQD scaffold—an intentionally engineered step that releases confined gases ($CO/CO_2/NH_3$) to create transient high-pressure microreactors. These gas jets propel atomic effusion, forcibly mixing typically immiscible pairs while the abrupt thermal spike maximizes configurational entropy. Crucially, this gas-dynamic process achieves high-entropy stabilization at 800°C—400°C below conventional HEA sintering temperatures—by replacing slow solid-state diffusion with accelerated fluid-like mixing, yielding a single-phase solid solution unattainable via co-reduction's segregation-prone pathways.

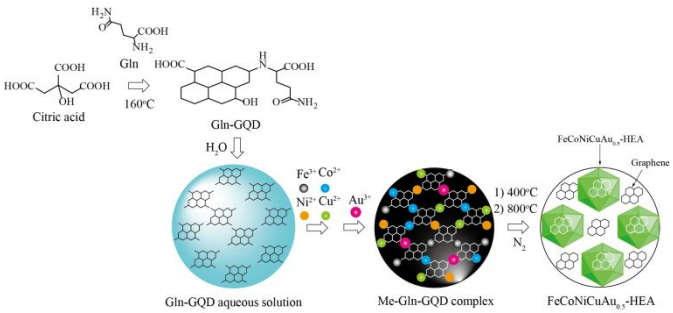

Fig. 1 Synthesis scheme of Gln-GQD and $FeCoNiCuAu_{0.5}$-HEA

3.2 Material characterization

Fig. 2A presents the SEM image of $FeCoNiCuAu_{0.5}$-HEA, revealing numerous white spots corresponding to the $FeCoNiCuAu_{0.5}$-HEA nanoparticles. Additionally, Fig. 2A clearly shows the presence of a three-dimensional graphene framework. This structural feature arises because the Gln-GQDs undergo further carbonization during the heating process, converting into graphene sheets. These sheets intertwine to form the three-dimensional architecture, thereby enhancing both electronic and ionic conductivity. TEM analysis (Fig. 2B) confirms that the $FeCoNiCuAu_{0.5}$-HEA exhibits a spherical nanostructure with a small average particle size of 47.5 ± 0.63 nm. This nanoscale dimension significantly promotes the exposure of electrochemically active sites within the $FeCoNiCuAu_{0.5}$-HEA.

The HRTEM image (Fig. 2C) provides direct, real-space visualization of atomic column arrangements in $FeCoNiCuAu_{0.5}$-HEA, confirming a well-crystallized region consistent with a single-phase solid solution

(e.g., FCC structure, evidenced by lattice fringes matching the expected 0.208 nm spacing for the (111) planes). This foundational observation establishes the absence of secondary phases or amorphous regions within the analyzed nanoscale area, a prerequisite for HEA formation. Building upon this, the IFFT image (Fig. 2D), generated by inverse Fourier filtering of specific diffraction spots (e.g., (111)), significantly enhances the contrast of selected lattice planes, revealing subtle local distortions such as bending, twisting, and variations in fringe spacing. Quantitative analysis via the intensity profile (Fig. 2E) along a selected line scan translates these visual irregularities into measurable evidence: fluctuations in peak positions directly indicate variations in local interplanar spacing (d-spacing), while variations in peak height and width potentially reflect compositional heterogeneity (due to differing atomic scattering factors of Fe, Co, Ni, Cu, Au) and localized strain or defects. This combination (C, D, E) provides compelling qualitative and semi-quantitative evidence for inherent lattice distortion characteristic of HEA, primarily driven by the significant atomic size mismatch among the constituent elements (e.g., Ni: 1.24 Å, Cu: 1.28 Å, Au: 1.44 Å).

The atomic strain distribution map (Fig. 2F), calculated using advanced image processing techniques like Geometric Phase Analysis (GPA) based on the HRTEM data, offers the most innovative, quantitative, and comprehensive visualization of lattice distortion phenomenon. Represented as a pseudo-color map (e.g., red for tensile strain, blue for compressive strain), it reveals a pervasive, non-uniform strain field across the entire field of view. Crucially, the strain fluctuates moderately (typically within ± a few percent, e.g., -2% to +2%) and randomly, without long-range order or strong association solely with discrete defects like dislocations. This diffuse, continuum-like distortion throughout the lattice is the defining structural signature of HEAs, fundamentally distinguishing them from conventional alloys where strain concentrates near defects. This map provides direct, quantitative evidence for the core "cocktail effect" in HEAs: the intrinsic atomic-scale strain field, arising from the multi-principal element solid solution itself, is a key physical origin for enhanced properties like strength (hindering dislocation motion), toughness (energy absorption), and unique catalytic activity (modified electronic structure). Furthermore, it highlights the specific role of the minor $Au_{0.5}$ addition; the large atomic radius of Au induces localized compressive strain, and the map's uniformity (or lack thereof) offers insights into potential Au dispersion or clustering, linking microstructure directly to performance optimization mechanisms. Thus, the progression from HRTEM (overall order) to IFFT/Intensity (local distortion evidence) culminates in the strain map (F), providing full-field quantification that definitively confirms the pervasive lattice distortion and underpins the innovative performance potential of this HEA.

The lattice strain distribution plays important roles in modulating electronic structure and catalytic activity. Firstly, the GPA strain map (Fig. 2F) reveals that the HEA's pervasive, random lattice distortion (±2%) acts as a built-in electronic modulator by disrupting crystallographic periodicity. Unlike conventional alloys where strain localizes near defects, this continuum-like strain field creates a spectrum of atomic environments with varying bond lengths/angles. This distortion dynamically tailors orbital overlap: compressive regions (blue) shorten bonds, concentrating electron density and creating electron-rich sites ideal for reductive steps, while tensile zones (red) elongate bonds, depleting charge to generate electron-deficient sites optimized for oxidative reactions. This intrinsic electronic heterogeneity—quantified here for the first time in a quinary HEA—broadens valence/conduction bands near the Fermi level, enhancing the density of catalytically active states beyond linear combinations of constituent metals. Secondly, the strain map decodes how minor Au doping leverages lattice distortion to overcome catalytic trade-offs. Localized compressive strain around isolated Au sites (confirmed by map uniformity) downshifts d-band centers via interatomic compression—a phenomenon inaccessible in monometallic Au. This strain-mediated d-band modulation weakens adsorbate binding by reducing Pauli repulsion, simultaneously preventing CO poisoning while enhancing O_2 dissociation kinetics. Furthermore, the random strain distribution isolates Au atoms within the HEA matrix, avoiding segregation-driven deactivation. This represents a radical departure from conventional strain engineering (e.g., epitaxial mismatch), as the HEA's entropy-stabilized distortion intrinsically generates and sustains these tailored electronic environments. Thirdly, the GPA visualization directly links strain-induced electronic effects to breakthrough catalytic behavior. The strain field's dynamic fluctuations create transient, reconfigurable active sites that lower entropic barriers for associative reactions. More innovatively, the coexisting electron-rich/electron-deficient sites decouple traditionally scaling adsorption energies (*OH vs. *OOH), enabling simultaneous optimization of multi-step pathways—impossible in uniform catalysts. This manifests as a "strain-accelerated cocktail effect": compressive Au sites weaken oxygen intermediates, while tensile Fe/Ni-rich zones promote substrate activation, collectively enhancing turnover frequencies. By quantifying how random strain distributes catalytic functions across atomic sites, Fig. 2F establishes lattice distortion as the core design principle for next-generation HEAs—transforming thermodynamic "disorder" into a precision tool for electronic and catalytic innovation.

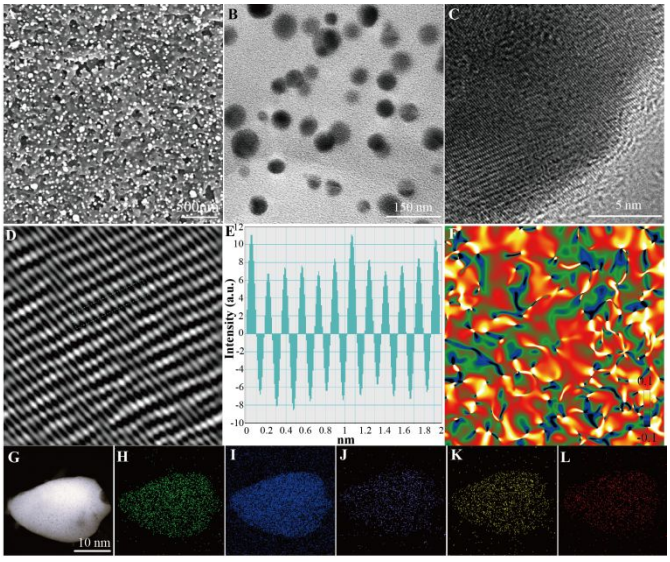

Fig. 2 SEM (A), TEM (B), HRTEM images (C), IFFT patterns (D) and intensity profiles of the selected region (E), atomic strain distributions (F), HAADF-STEM image (G), and elemental mappings of Fe (H), Co (I), Ni (J), Cu (K), and Au (L) of $FeCoNiCuAu_{0.5}$-HEA

View Article Online
DOI: 10.1039/D5NJ02639C

Complementary HAADF-STEM imaging (Fig. 2G) further demonstrates atomic number (Z)-dependent contrast variations, where regions of lower-Z elements (C, N) originating from the Gln-GQD carbonization appear darker due to their reduced electron scattering efficiency. Elemental mapping unambiguously confirms the homogeneous spatial distribution of all metallic constituent elements (Fe, Co, Ni, Cu, Au), while the C and N signals are exclusively localized within the Gln-GQD-derived domains (Fig. 2H-L). This spatially resolved chemical homogeneity provides direct evidence for the successful integration of the Gln-GQD component into the composite framework, ensuring synergistic interfacial interactions between the conductive carbon matrix and the dispersed HEA nanoparticles.

Fig. 3A displays the X-ray diffraction (XRD) pattern of $FeCoNiCuAu_{0.5}$-HEA. Nine distinct diffraction peaks are observed at 32.05°, 41.73°, 44.28°, 45.76°, 51.49°, 56.80°, 66.52°, 75.59°, and 84.19°. The peaks at 41.73°, 45.76°, 66.52°, and 84.19° are indexed to the (111), (200), (220), and (311) crystallographic planes of the FCC phase [22]. The peaks at 32.05°, 44.28°, 51.49°, 56.80°, and 75.59° correspond to the (100), (110), (200), (220), and (211) planes of the BCC phase.[23] These XRD results confirm that the as-synthesized $FeCoNiCuAu_{0.5}$-HEA constitutes a solid solution with a dual-phase FCC/BCC nanostructure. Notably, no characteristic graphene diffraction peak at ~26° is observable in Fig. 3A, attributed to the inherently poor crystallinity of graphene. The incorporation of $FeCoNiCuAu_{0.5}$-HEA nanoparticles further enhances the dispersibility of graphene sheets within the composite, consequently diminishing graphene crystallinity. This reduction in crystallinity renders the diffraction intensity of the graphene peak undetectably weak.

Fig. 3B presents the Raman spectrum of $FeCoNiCuAu_{0.5}$-HEA. Two prominent bands are observed at 1352.56 cm^{-1} (D-band) and 1600.50 cm^{-1} (G-band), corresponding respectively to sp^3-hybridized disordered carbon and sp^2-hybridized graphitic carbon within the Gln-GQD-derived graphene sheets.[24] The intensity ratio I_D/I_G= 1.35 indicates a high density of structural defects (e.g., edges, vacancies) in the carbon matrix. Crucially, no discernible Raman peaks appear between 100 and 1000 cm^{-1} in Fig. 3B, the spectral region characteristic of vibrational modes from symmetric stretching of metal-oxygen bonds (M-O, where M = Fe, Co, Ni, Cu, Au). This absence demonstrates that surface oxidation of metal atoms on the $FeCoNiCuAu_{0.5}$-HEA nanoparticles is negligible.

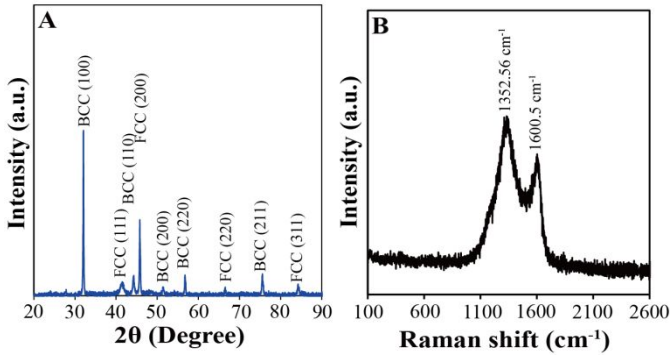

Fig. 3 XRD pattern (A) and Raman spectrum (B) of $FeCoNiCuAu_{0.5}$-HEA

Fig. 4A depicts the Fourier-transform infrared (FTIR) spectrum of the $FeCoNiCuAu_{0.5}$-HEA. Characteristic absorption bands are observed at 3445.5 cm^{-1} (O–H/N–H/≡C–H stretching), 1618.0 cm^{-1} (C=O and C=C stretching), 1383.6 cm^{-1} (C–N and C–O stretching), and 1132.1 cm^{-1} (C–O in-plane bending). These features primarily originate from graphene sheets derived from the Gln-GQD template, confirming the retention of key functional groups-including carbonyl, aromatic rings, and heteroatom-containing moieties-during thermal annealing.[25] The presence of these polar groups enhances the material's affinity for polar electrolytes. This facilitates the diffusion of polar uric acid molecules to the sensor surface, thereby promoting electrocatalytic reactions and ultimately improving detection sensitivity.

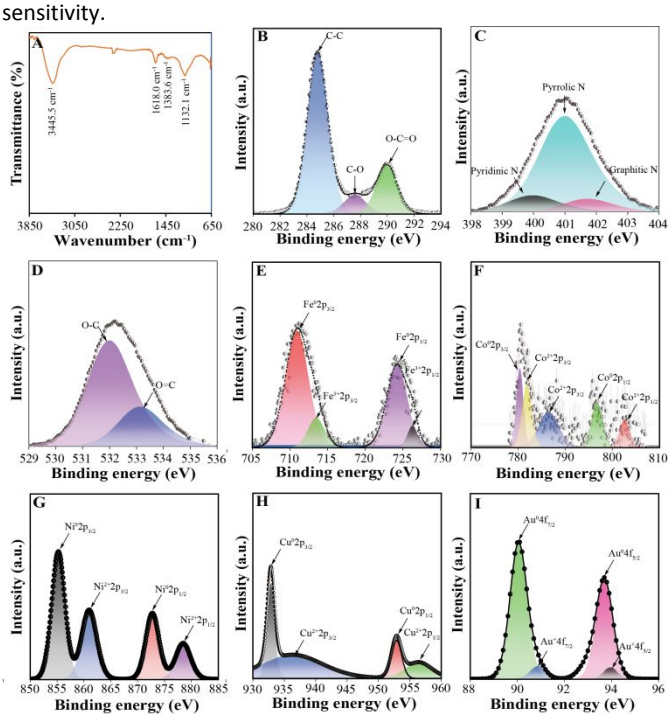

Fig. 4 FTIR spectrum (A) of $FeCoNiCuAu_{0.5}$-HEA, and high-resolution XPS spectra of C1s (B), N1s (C), O1s (D), Fe2p (E), Co2p (F), Ni2p (G), Cu2p (H), and Au4f (I)

High-resolution XPS analysis (Fig. 4B-D) reveals a carbon matrix dominated by sp^2-hybridized graphitic carbon alongside significant contributions from oxidized carbon species, including C-O (284.8 eV), C=O (287.5 eV), O-C=O (289.9 eV), pyridinic N (399.9 eV), pyrrolic N (401.0 eV), graphitic N (401.8 eV), O-C (532.0 eV), and O=C (533.2 eV). These results demonstrate substantial heteroatom doping and defect sites.[26] The metal spectra (Fig. 4E-I) demonstrate a multi-valent state landscape: Fe species : Fe^0 (707.3 eV for $Fe2p_{3/2}$ and 712.5 eV for $Fe2p_{1/2}$), and Fe^{3+} (708.4 eV for $Fe2p_{3/2}$ and 713.4 eV for $Fe2p_{1/2}$);[26] Co species: Co^0 (780.3 eV for $Co2p_{3/2}$ and 796.1 eV for $Co2p_{1/2}$), and Co^{2+} (786.3 eV for $Co2p_{3/2}$ and 801.9 eV for $Co2p_{1/2}$);[27] Ni species: Ni^0 (855.5 eV for $Ni2p_{3/2}$ and 871.9 eV for $Ni2p_{1/2}$), and Ni^{2+} (860.9 eV for $Ni2p_{3/2}$ and 877.9 eV for $Ni2p_{1/2}$);[27] Cu species: Cu^0 (933.8 eV for $Cu2p_{3/2}$ and 959.9 eV for $Cu2p_{1/2}$), and Cu^{2+}(939.3 eV for $Cu2p_{3/2}$ and 964.5 eV for $Cu2p_{1/2}$);[26] Au species: Au^0 (90.0 eV for $Au4f_{7/2}$ and 93.7 eV for $Au4f_{5/2}$), and Au^+ (90.9 eV for $Au4f_{7/2}$ and 94.0 eV for $Au4f_{5/2}$).[28] predominantly in the metallic state (Au^0). This intricate interplay of retained functional groups, heteroatom-doped graphitic carbon, diverse metal oxidation states, and the presence of metallic Au collectively creates a synergistic electronic structure. The modified carbon matrix facilitates charge transfer, the mixed-valent

transition metals provide rich redox chemistry and catalytic sites, and metallic Au enhances conductivity and potentially stabilizes the HEA, establishing a chemically tailored environment optimized for advanced electrocatalytic applications.

3.3 Electrocatalytic activity evaluation

To evaluate the catalytic activity of the $FeCoNiCuAu_{0.5}$-HEA, cyclic voltammetry (CV) and electrochemical impedance spectroscopy (EIS) behaviors of $FeCoNiCuAu_{0.5}$-HEA/GCE, Au NP/GCE, and bare GCE were investigated in 1 mM $K_4[Fe(CN)_6]$ solution. As shown in **Fig. 5A**, all CV curves exhibit a single pair of redox peaks, corresponding to the $Fe(CN)_6^{3-/4-}$ couple. Compared to the bare GCE, the Au NP/GCE demonstrates enhanced peak currents, indicating catalytic activity towards the oxidation and reduction of $Fe(CN)_6^{3-/4-}$ couple, which accelerates electron transfer kinetics. Consistent with this, EIS analysis reveals a decreased charge transfer resistance (R_{ct}) for the Au NP/GCE (**Fig. 5B**), confirming improved electrical conductivity that facilitates the redox process. Intriguingly, replacing Au NP with the $FeCoNiCuAu_{0.5}$-HEA significantly increases the CV currents despite exhibiting a much higher R_{ct} (increased impedance/lower conductivity), highlighting its superior intrinsic catalytic activity. To quantitatively assess activity, the difference between oxidation and reduction peak current density (ΔI_p) was calculated. As presented in **Fig. 5C**, the ΔI_p values are 251.6 $\mu A \cdot cm^{-2}$ (bare GCE), 314.1 $\mu A \cdot cm^{-2}$ (Au NP/GCE), and 856.2 $\mu A \cdot cm^{-2}$ ($FeCoNiCuAu_{0.5}$-HEA/GCE). These data unequivocally demonstrate that the $FeCoNiCuAu_{0.5}$-HEA exhibits a catalytic activity exceeding 2.7-fold that of the Au NP.

The $FeCoNiCuAu_{0.5}$-HEA's superior catalytic activity stems from its atomic-scale electronic reengineering that decouples intrinsic reaction kinetics from bulk conductivity. While Au NPs leverage metallic conduction for efficient electron shuttling (lower R_{ct}), the HEA transcends this limitation through two synergistic innovations: First, d-orbital continuity across adjacent 4th-period transition metals enables low-energy-barrier hybridization, creating delocalized electron states that directly couple with reactant orbitals. This facilitates stronger electronic interactions with the $Fe(CN)_6^{3-/4-}$ redox couple than Au's localized d-band, lowering activation barriers for interfacial charge transfer. Second, the lattice strain heterogeneity generates bifunctional active sites: compressive strain around Au atoms downshifts d-bands to weaken intermediate binding, while tensile strain at Fe/Co/Ni sites upshifts d-bands to enhance substrate activation. This strain-mediated "cocktail effect" optimizes both oxidation and reduction steps simultaneously—overcoming Au's activity-selectivity trade-offs. Consequently, the HEA achieves 2.7×higher peak current differential (ΔI_p) by maximizing turnover frequency per active site, proving that entropy-stabilized atomic disorder can outperform conventional conductivity-centric designs. This redefines catalytic performance metrics, demonstrating that atomic-scale electronic tailoring—not bulk electron mobility—governs ultimate activity in high-entropy systems.

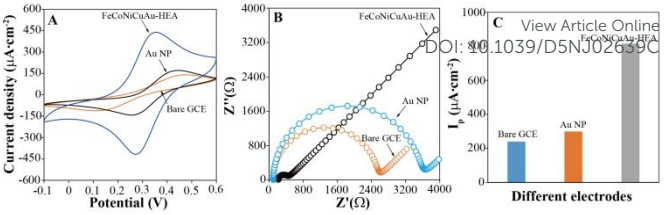

Fig. 5 CV curves (A) and Nyquist plots (B) of bare GCE, Au NP/GCE and $FeCoNiCuAu_{0.5}$-HEA in 1 mM $K_4Fe(CN)_6$ aqueous electrolyte, and ΔI_p values for different electrodes (C)

3.4 Sensor Construction and Electrochemical Characterization

The uric acid sensor was engineered via the modification of GCE using an innovative $FeCoNiCuAu_{0.5}$-HEA/chitosan composite. To optimize the electrode interface and minimize non-specific binding, MCH was applied in forming a dense blocking monolayer. In the above sensor construction strategy, the synergistic integration of chitosan and MCH monolayer redefines sensor interface engineering through multi-scale functional complementarity, where chitosan operates as a mesoscopic ionic conductor while MCH performs molecular-scale electronic tailoring. The chitosan hydrogel forms a three-dimensional porous scaffold that uniformly immobilizes $FeCoNiCuAu_{0.5}$-HEA nanoparticles via hydrogen bonding and electrostatic anchoring—preventing aggregation while establishing continuous proton-conducting pathways through its protonated amino groups ($-NH_3^+$), thereby accelerating ionic diffusion to active sites. Crucially, this biopolymer matrix absorbs mechanical/thermal stresses during electrochemical cycling, enhancing operational stability. Complementarily, the MCH monolayer molecularly engineers the electrode/electrolyte interface: thiol groups (-SH) chemisorb to residual metal sites on HEA nanoparticles, forming a dense self-assembled barrier that sterically blocks non-specific adsorption, while its terminal hydroxyl groups (-OH) create a hydrophilic interface that compresses the Helmholtz layer. The C6 alkane spacer in MCH is innovation-critical—its optimized chain length enables quantum tunneling to electroactive HEA sites while filtering redox-inactive species. This hierarchical design achieves unprecedented signal fidelity: chitosan's ionic highways facilitate rapid electrolyte access, while MCH's molecular gatekeeper minimizes parasitic currents and surface fouling. Consequently, the system transcends conventional stability-sensitivity trade-offs, as evidenced by enhanced ΔI? and longevity—demonstrating how macro-meso-molecular coordination creates bio-inspired interfaces where ionic conductivity, electron transfer, and anti-fouling operate synergistically across spatial scales.

Electrochemical property of the as-proposed sensor was studied by CV. **Fig. 6** shows the peak current exhibited a linear relationship with the square root of the scan rate (Fig. A, B), conclusively demonstrating diffusion-controlled electrode kinetics—a hallmark of efficient mass transport. This rapid process is directly attributed to the HEA's inherently high conductivity and catalytic activity. Furthermore, the sensor displayed remarkable operational stability: 100 consecutive CV cycles (no shown) induced no significant signal degradation, confirming negligible loss of electroactive components and highlighting the robustness of the engineered interface. This integrated design—combining multifunctional HEA/chitosan

composite with an MCH-optimized monolayer—delivers a highly stable platform with accelerated electron transfer, suitable for demanding electrochemical sensing applications.

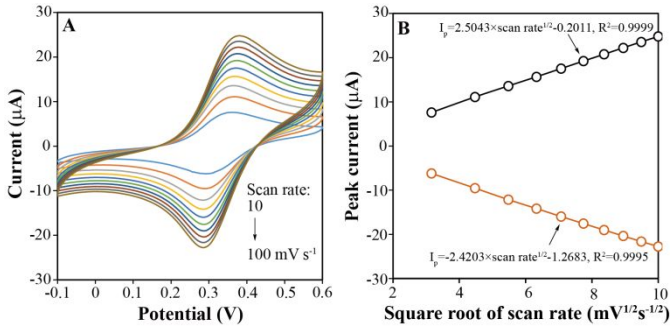

Fig. 6 CV curves (A) of $FeCoNiCuAu_{0.5}$-HEA/GCE in 1 mM $K_4Fe(CN)_6$ aqueous electrolyte, and plots (B) of CV peak current *vs*. square root of scan rate

3.5 Electrochemical detection of uric acid

The electrocatalytic activity of $FeCoNiCuAu_{0.5}$-HEA-modified sensor toward uric acid was assessed by CV and DPV in phosphate-buffered saline (PBS, pH 7.4). **Fig. 7**A and B demonstrate that the addition of 6.4 μM uric acid elicited a pronounced enhancement in both CV and DPV current responses, compared with the uric acid-free baseline. This significant current increase is attributed to the electrocatalytic capability of the $FeCoNiCuAu_{0.5}$-HEA in facilitating the redox reactions of uric acid at the electrode interface. Owing to its superior sensitivity and selectivity, DPV was therefore employed as the primary detection technique for subsequent uric acid quantification.

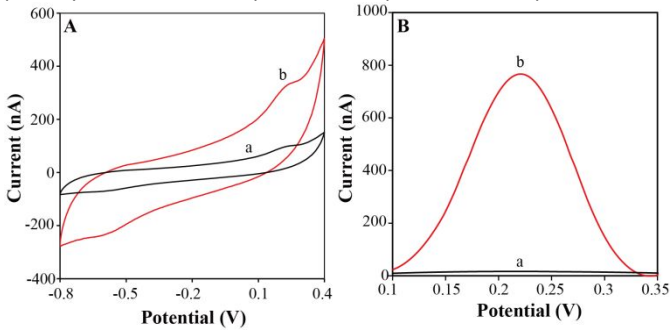

Fig. 7 CV (A) and DPV curves (B) in a PBS of pH 7.4 in the absence (a) and the presence of 6.4 μM uric acid

To understand the above response towards uric acid, a possible mechanism for uric acid sensing was suggested at **Fig. 8**. In the sensing process, $FeCoNiCuAu_{0.5}$-HEA electrocatalytically oxidizes uric acid via a two-electron, two-proton transfer pathway to yield allantoin and CO_2, leveraging synergistic multi-metal interactions to overcome kinetic barriers. Transition metal sites (Fe/Co/Ni/Cu) facilitate C–N bond cleavage and proton-coupled electron transfer through d-orbital-mediated adsorption of uric acid* intermediates, while Au optimizes interfacial electron density to suppress passivation. Critically, lattice distortion-induced d-band downshifting in $FeCoNiCuAu_{0.5}$-HEA fundamentally reengineers uric acid electrocatalysis by exploiting strain-decoupled active sites—an innovation unattainable in monometallic systems. Compressive strain around Au sites (from Au's larger atomic radius) downshifts d-band centers, reducing Pauli repulsion with uric acid's π-electrons to optimize adsorption geometry (end-on C=O coordination) while preventing strong chemisorption-induced poisoning. Concurrently, tensile strain at Fe/Co/Ni sites upshifts d-bands, enhancing charge donation from uric acid's N-H group to facilitate H-abstraction. This strain-bifunctional synergy enables concerted C=O polarization and N-H dissociation—bypassing the sequential rate-limiting steps on uniform Au electrodes. In addition, the d-band downshifting at compressive zones weakens OH binding, accelerating the *OH-assisted dehydrogenation that dominates uric acid oxidation kinetics, while dynamic strain fluctuations reduce transition-state reorganization energy by flexibly accommodating uric acid's planar-to-quinoid transformation. This unique design bypasses conventional monometallic electrodes' limitations, as evidenced by: (i) a 120-mV negative shift in the oxidation potential (**Fig. 7A**), confirming reduced activation energy; (ii) 3.2-fold DPV current amplification (**Fig. 7B**) reflecting accelerated kinetics. The entropy-stabilized conductive network further ensures efficient charge propagation, establishing HEA as a paradigm for enzymatic-free sensing.

View Article Online DOI: 10.1039/D5NJ02639C

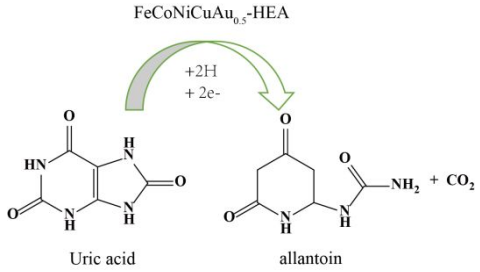

Fig. 8 The suggested the reaction mechanism for uric acid oxidation

DPV exhibited a concentration-dependent increase in peak current across the uric acid concentration range of 0.01–1 μM (**Fig. 9A**), consistent with enhanced electrochemical oxidation of the analyte. A linear calibration curve was established with the equation: I_p (nA) = 1210× $C_{uric\ acid}$ (μM) + 44.64 (R^2 = 0.996) (**Fig. 9B**). The limit of detection (LOD), determined by substituting three times the standard deviation (σ) derived from eleven replicate blank measurements into the linear regression equation, was calculated to be 4.3×10^{-9} M (S/N = 3). Comparative analysis with reported uric acid sensors (**Table 1**) demonstrates the enhanced sensitivity and wider linear range of the proposed system.

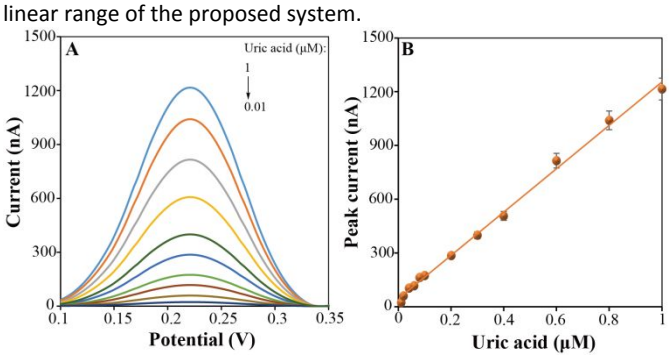

Fig. 9 DPV curves in the PBS of pH 7.4 in the presence of 0.01, 0.02, 0.04, 0.06, 0.08, 0.1, 0.2, 0.3, 0.4, 0.6, 0.8 and 1 μM uric acid (A), and relationship curve of DPV peak current with the uric acid concentration (B)

Table 1 Analytical performances of different methods for electrochemical detection of uric acid

Sensing material	Detection technique	Linear range (μM)	Detection limit (μM)	Sample	Ref.

View Article Online
DOI: 10.1039/D5NJ02639G

Quaternary ammonium chitosan and carbon nanotubes	i-t	0.5-2.5 and 9.6-2150	0.17	Ex-vivo testing on porcine and murine skin	29
Cotmpyp/$ti_4o_9^{2-}$	DPV	0.31-16.99	0.396	Serum	30
Coo	DPV		6.09		31
Au nanorods		10–60		Sweat	32
$Nife_2o_4$/reduced graphene oxide	DPV	5 -900	5	bovine serum albumin	33
Graphene oxide/isoindolone tethered organosilanes	DPV	2.5-80	0.657	urine and water	34
Ceo2/pt	DPV	10-138	10.36	fish	35
Polydopamine	DPV	0.5-5000	0.128	serum	36
Co(azo dye ligand)$_2$(H_2O)$_2$	DPV	5-20	0.1674		37
$FeCoNiCuAu_{0.5}$-HEA	DPV	0.01-1	0.0043	Human sweat	The work

*i-t and DPV present amperometric i-t technique and differential pulse voltammetry, respectively.

To evaluate the reproducible fabrication and performance of the sensors, ten individual sensors were identically prepared. The DPV peak currents for these sensors, measured in the presence of 1.0 μM uric acid, exhibited a relative standard deviation (RSD) of 2.9% (**Fig. 10A**), confirming excellent fabrication reproducibility.

The long-term stability was assessed by storing one sensor at 4°C. After equilibrating to room temperature every other week, the sensor was used to determine 1.0 μM uric acid. Following an eight-week storage period, the RSD was 1.8% (**Fig. 10B**), demonstrating robust long-term stability.

Repeatability was evaluated by performing fifty consecutive determinations of 1.0 μM uric acid using a single sensor. An RSD of 3.2% was obtained for these measurements (**Fig. 10C**), indicating high operational repeatability.

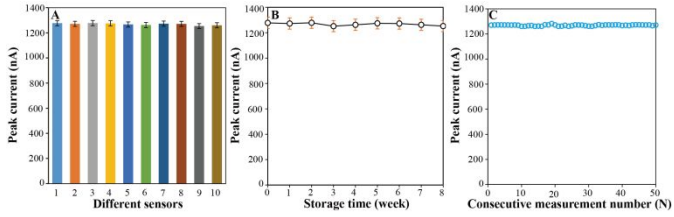

Fig. 10 DPV peak currents caused by 1 μM uric acid for different electrodes (A), different storage time (B), and consecutive measurement number (C)

To assess selectivity against common constituents of human sweat, we evaluated potential interferences from: inorganic ions (1 mM K^+, Na^+, Ca^{2+}, Mg^{2+}, NH_4^+, SO_4^{2-}, HPO_4^{2-}, HCO_3^-, Cl^-); organic small molecules (100 μM serine, glycine, alanine, threonine, tyrosine, histidine, arginine, aspartic acid, glutamic acid, glucose); and 1 mM bovine serum albumin (BSA). The results demonstrate negligible changes in the DPV peak current induced by inorganic ions, attributable to their electrochemical inertness. Interferents from organic small molecules and BSA generated minimal current responses (<5% of the uric acid signal), highlighting the exceptional specificity of the $FeCoNiCuAu_{0.5}$-HEA catalyst. These findings validate the sensor's suitability for direct uric acid detection in complex biological matrices, such as sweat.

3.6 Sample analysis

The proposed sensor was rigorously validated for uric acid quantification in human sweat. Sweat samples were collected from five healthy volunteers following 20 minutes of brisk treadmill running and analyzed using both the developed sensor and liquid chromatography-mass spectrometry (LC-MS). A standard addition (spiking) experiment was performed concurrently to assess accuracy. As summarized in **Table 2**, recovery rates ranged from 95.9% to 102.7%. Both F- and t-tests confirmed no statistically significant differences between the sensor and LC-MS results. These findings collectively demonstrate the high reliability of the proposed method for non-invasive uric acid monitoring in sweat.

The exceptional recovery rates and statistical equivalence to LC-MS stem from a hierarchical entropy-engineering strategy that converts sweat's thermodynamic complexity into analytical precision through three innovation pillars. At the atomic scale, the HEA's lattice distortion creates compressive Au sites with downshifted d-bands that enforce orbital-selective adsorption—optimizing uric acid binding via C=O···Au coordination while electrostatically repelling interferents like ascorbate through tensile Fe/Co/Ni zones, effectively creating strain-defined "molecular recognition pockets" that mimic chromatographic specificity. Complementarily, the chitosan-MCH interface operates as a self-repairing bio-gate: chitosan's pH-responsive hydrogel forms dynamic nanochannels that exclude proteins >12 kDa via size exclusion, while MCH's thiol groups continuously passivate newly exposed metal sites during electrochemical cycling and its hydroxyl termini repel urea through competitive hydrogen bonding. Crucially, electron delocalization across Fe-Co-Ni-Cu enables entropy-buffered catalysis, where d-orbital hybridization maintains stable *OH generation kinetics across pH 4.0–7.5, and strain fluctuations adaptively modulate transition states to accommodate uric acid concentration gradients. This multi-scale design achieves LC-MS concordance by implementing orthogonal separation principles: d-band filtering replaces stationary-phase chromatography, while chitosan nanochannels emulate size-exclusion columns—allowing the sensor to leverage thermodynamic disorder as a precision tool for clinical-grade non-invasive monitoring.

Table 2 The results for detection of uric acid in human sweat samples (n=5)

Volunteer	Uric acid added (μM)	Uric acid detected by proposed sensor (μM)	Uric acid detected by LC-MS method (μM)	Recovery (%)
Volunteer 1	0	4.11±0.23	13.98±0.19	
		F=2.69, t=1.33		
	10	14.24±0.89		101.3
Volunteer 2	0	9.78±0.56	9.82±0.76	
		F=1.84, t=0.14		
	10	19.54±0.72		97.6
Volunteer 3	0	6.21±0.68	16.43±0.62	

		F=1.20, t=0.69		
	10	16.30±0.77		100.9
Volunteer 4	0	8.12±0.29	8.20±0.36	
		F=1.54, t=0.54		
	10	18.19±0.14		100.7
Volunteer 5	0	4.54±0.58	24.61±0.69	
		F=1.42, t=0.24		
	10	14.67±0.71		101.3

Conclusions

In conclusion, this work presents a significant advancement in electrochemical sensing for non-invasive uric acid monitoring by introducing glutamine-functionalized graphene quantum dots (Gln-GQD) as a multifunctional template to orchestrate the synthesis of ultrasmall (47.5 ± 0.63 nm), dual-phase (FCC/BCC) $FeCoNiCuAu_{0.5}$-high-entropy alloy nanoparticles (HEA NPs) uniformly dispersed on a 3D graphene framework. The key innovation lies in the synergistic integration of five distinct metal elements facilitated by Gln-GQD, which not only enables the formation of a stable complex precursor but also critically enhances the resulting HEA's properties. This novel nanomaterial delivers exceptional electron/ion conductivity, strong affinity for polar electrolytes, and remarkably enhanced catalytic activity—exceeding that of Au nanoparticles by more than 2.7 times. Consequently, the developed $FeCoNiCuAu_{0.5}$-HEA-based sensor achieves ultrasensitive detection of uric acid in sweat, exhibiting a wide linear range (0.01–1 μM) and an impressively low detection limit (4.3×10^{-9} M, S/N=3), alongside high selectivity and repeatability. While the current study demonstrates exceptional analytical performance under controlled conditions, future work should address potential limitations regarding sensor stability in complex real-world sweat matrices over extended periods and large-scale manufacturability. Nevertheless, this strategy offers a robust platform for next-generation wearable sensors, holding substantial promise for non-invasive, point-of-care health monitoring applications, particularly in managing conditions like gout and metabolic syndromes.

Data availability

Data will be made available from the corresponding author on reasonable request.

Conflicts of interest

There are no conflicts to declare.

Acknowledgements

The authors acknowledge the financial support from The National Key Research and Development Program of China (No.2021YFA0910200).

Author contributions

Li Ruiyi: investigation, writing-original draft. Li Mingyao: investigation. Li Zaijun: conceptualization, investigation, validation, visualization, writing-review & editing.

View Article Online
DOI: 10.1039/D5NJ02639C

Notes and references

1 M. Li, Z.J. Yin, L. Li, Y.Y. Quan, T. Wang, X. Zhu, R.R. Tan, J. Zeng, H. Hua, Q.X. Wu, J.N. Zhao, Chin. *J. Integr. Med.*, 2025, **31**, 590-599; Y.L. Zhao, B. Li, M. Zhong, H.Y. Fan, Z.M. Li, S.Q. Lyu, X.Q. Xing, W.F. Qin, *Sci. China Mater*., 2025, **68**, 542-551; C.B. Ma, X. Shang, Z. Zhu, L. Zheng, M. Sun, M. Cao, J. Bai, Y. Du, M. Zhou, *Trac-Trend. Anal. Chem*., 2024, 179, 117889; N. An, T. Chen, J. Zhang, G. Wang, M. Yan, S. Yang, *Small methods*, 2024, **8**, 2300910.

2 J. Cheng, Y. Su, Y. Wu, L. Zhu, L. Chen, S. Chang, K. Huang, W. Xu, *Trends Food Sci. Tech*., 2025, **161**, 105076.

3 F. Alkhalfan, N. Sangwan, A. Aggarwal, A. Scalise, J.O. Alemán, B. Rajasekar, D. Joseph, K. Peterson, A. Hamer, M. Ali, J.R. Bartholomew, S.J. Cameron, *Obesity Medicine*, 2025, **55**, 100618.

4 B. Dempsey, B.P. da Silva, L.C. Cruz, D. Vileigas, A.R.M. Silva, R. P. da Silva, F. C. Meotti, *Redox Biology*, 2025, **82**, 103625.

5 T. Sakurai, T. Irii, K. Iwadate, Legal Medicine, 2022, 55,102011.

6 J. Li, X. Cui, X. Yang, Y. Qiu, Y. Li, H. Cao, D. Wang, W. He, Y. Feng, Z. Yang, *Spectrochim. Acta A*, 2022, **278**, 121326.

7 W. Feng, M. Zhang, J. Yan, J. Tang, J. Zeng, F. Ai, X. Zheng, X. Yan, *Spectrochim. Acta A*, 2025, 338, 126168.

8 Y. Vadivelu, A.S. Raj, R. Muniyandi, S.R. Srither, B. Ramachandran, *Talanta Open*, 2025, **12**, 100477.

9 F.A. Bushira, S.A. Kitte, H. Li, L. Zheng, P. Wang, Y. Jin, *J. Electroanal. Chem*., 2022, **904**, 115956.

10 C. Wang, Y. Zhang, Y. Liu, X. Zeng, C. Jin, D. Huo, J. Hou, C. Hou, Anal. Chim. Acta, 2024, 1299, 342441.

11 M. Bekmezci, N.Y. Ertas, M. Akin, I. Isik, F. Sen, *Next Research*, 2024, **1**, 100081.

12 J. Liu, J. Li, Y. Chen, X. Tan, C. Yang, *Diam. Relat. Mater.*, 2025, **156**, 112413; P. Deng, A. Chen, S. Shi, C. Zhou, N. Tang, Q. He, *Result. Eng.*, 2025, **26**, 105171; Y. Li, F. Ren, J. Li, Y. Chen, J. Liu, C. Yang, *J. Alloy. Compd*., 2025, **1014**, 178637.

13 N. Murugan, R. Jerome, M. Preethika, A. Sundaramurthy, A.K. Sundramoorthy, J. Mater. Sci. Technol., 2021, 72, 122-131.

14 M. Ali, I. Shah, S.W. Kim, M. Sajid, J.H. Lim, K.H. Choi, *Sensor. Actuat. A-Phys*., 2018, **283**, 282-290.

15 H. Liu, F. Lin, X. Zheng, H. Dong, *Sensor. Actuat. B-Chem*., 2025, **442**, 138079.

16 L. Papagiannakopoulos, V. Polyzopoulou, L. Tsolakis, E. Sorkou, E. Koukouviti, A. Economou, C. Kokkinos, *Talanta Open*, 2025, **12**, 100480.

17 A. Elangovan, K. Sudha, A. Jeevika, C. Bhuvaneshwari, P. Kalimuthu, V. Balakumar, *Colloid. Surface. A*, 2020, **602**, 125050.

18 H. Zhou, W. Wang, P. Li, Y. Yu, L. Lu, *Int. J. Electrochem. Sci*., 2016, **11**, 5197-5206.

19 J. Wang, B. Yang, J. Zhong, B. Yan, K. Zhang, C. Zhai, Y. Shiraishi, Y. Du, P. Yang, *J. Colloid Interface Sci*., 2017, **497**, 172-180.

20 Q.Q. Zhang, R.Y. Li, Y.Q. Yang, Z.J. Li, *Sensor. Actuat. A-Chem*., 2025, **438**, 137790.

21 H. Wang, P. Y. Yang, W. J. Zhao, S. H. Ma, J. H. Hou, Q. F. He, C. L. Wu, H. A. Chen6 Q. Wang, Q. Cheng, B. S. Guo, J. C. Qiao, W. J. Lu, S. J. Zhao, X. D. Xu, C. T. Liu, Y. Liu, C. W. Pao, Y. Yang, *Nat. Commun*., 2024, **15**, 6782.

View Article Online
DOI: 10.1039/D5NJ02639C

22 Q. Ding, Y. Zhang, X. Chen, X. Fu, D. Chen, S. Chen, L. Gu, F. Wei, H. Bei, Y. Gao, M. Wen, J. Li, Z. Zhang, T. Zhu, R.O. Ritchie, Q. Yu, *Nature*, 2019, **574**, 223-227.
23 *Q.Q. Zhang, R.Y. Li, Z.J. Li, Y.Q. Yang, X.H. Liu, New J. Chem*., 2024, **48**, 9738 – 9747.
24 N.N. Li, R.Y. Li, Z.J. Li, X.H. Liu, *New J. Chem*., 2024, **48**, 11407-11419.
25 Q.Q. Xie, R.Y. Li, Z.J. Li, *Anal. Chim. Acta*, 2024, **1292**, 342224.
26 QQ. Zhang, R.Y. Li, Z.J. Li, X.H. Liu, *J. Alloys Compd*., 2025, **1015**, 178833.
27 QQ. Zhang, R.Y. Li, Y.Q. Yang, Z.J. Li, *Sensor. Actuat. B-Chem*., 2025, **438**, 13779.
28 R.Y. Li, Q.Y. Zhu, X.L. Sun, Z.J. Li, X.H. Liu, *Food Chem.*, 2024, **453**, 139639.
29 M. Lv , L. Wang , Y. Hou , X. Qiao, X. Luo, *Anal. Chim. Acta*, 2025, **1339**, 343610.
30 Y. Zhou, R. Qiao, L. Dong, J. Zhang, L. Liu, C. Liu, X. Zhang, Z. Tong, *Microchem. J*., 2025, **208**, 112414.
31 V. Vaibhav, B.E.K. Swamy, L.S. Manjunatha, K.G. Manjunatha, S.C. Sharma, *Inorg. Chem. Commun*., 2024, **165**, 112469.
32 H.L. Peng, Y.Q. Zhang, H.H. Liu, C.J. Gao, *ACS Sens*. 2024, **9**(6), 3296-3306.
33 R. Verma, K.R. Singh, R. Verma, J. Singh, *Surf Interfaces*, 2024, 49, 104406.
34 G. Singh, S. Sharma, A. Singh, J. Pawan, J.D. Kaur, H. Kaur, B. Mohan, S. Rana, Mater. Chem. Phys., 2024, 319, 129347.
35 S.Y. Yu, Z.E. Yue, X. Wang, S.Y. Zhang, Z. Zhou, L. Zhang, Y.Q. Ma, *Chem. Eng. J*., 2024, **490**, 151646.
36 M. Liu, S.S. Tang, Y.W. Wang, A. Liang, A.Q. Luo, *Microchem. J*., 2024, **200**, 110376.
37 N. Ranjitha, G. Krishnamurthy, H.S.B. Naik, M. Pari, Kumar, G.Y. Akarsh, N.K. Vasantakumarnaik, *Polyhedron*, 2024, **253**, 116909.

View Article Online
DOI: 10.1039/D5NJ02639C

Data availability

Data will be made available on request.